

## The three-dimensional flow organization past a micro-ramp in a supersonic boundary layer

Z. Sun,<sup>a)</sup> F. F. J. Schrijer, F. Scarano, and B. W. van Oudheusden

*Aerospace Engineering Department, Delft University of Technology,  
Kluyverweg 1, 2629HS Delft, The Netherlands*

(Received 10 October 2011; accepted 23 March 2012; published online 16 May 2012)

The three-dimensional instantaneous flow organization in the near wake of a micro-ramp interacting with a Mach 2.0 supersonic turbulent boundary layer is studied using tomographic particle image velocimetry. The mean flow reveals a wake with approximately circular cross section dominated by a pair of counter-rotating streamwise vortices generating a focused upwash motion at the symmetry plane. In the instantaneous flow organization a flow instability of Kelvin-Helmholtz (K-H) type is observed in the shear layer between the wake and outer flow. Intermittent arc-shaped vortices are visualized that locally accelerate the outer fluid and further decelerate the inner region. The streamwise vortex pair displays an undulating behavior. Their interaction with the K-H vortices considerably increases the overall complexity of the wake. It appears that the streamwise vortex filaments under the K-H vortex train approach each other due to the focused ejection activity resulting from the K-H vortex. The statistical properties of turbulent fluctuations yield maximum activity at the core of the streamwise vortex and within the upwash region, and the Reynolds stresses peak within the shear layer. The topological organization of the wake vortices is formulated through a conditional average over the vorticity field. © 2012 American Institute of Physics. [<http://dx.doi.org/10.1063/1.4711372>]

### I. INTRODUCTION

The micro-ramp vortex generator is a device intended for the passive control of boundary layer flows. It has been receiving research interests because of its attributed ability of reducing flow separation caused by shock wave boundary layer interaction (SWBLI), which is encountered in numerous aerospace applications, such as supersonic inlets and propulsion-wing or propulsion-fuselage interactions. Bleeding is the conventional approach of boundary layer control for performance improvement in the supersonic inlet.<sup>1</sup> However, with the extraction of a considerable amount of low momentum fluid in the near wall region, a larger inlet area is required at the expense of additional drag and weight in addition to other disadvantages. Micro-ramps with a height less than the boundary layer thickness interact with the lower momentum layer of flow and their effect concentrates on the most turbulent part of the boundary layer. They have been recently proposed as a novel type of boundary layer control technique because they appear to maintain effectiveness in reducing flow separation while producing a smaller drag increase when compared to larger conventional ramps. Many efforts have so far already been devoted to evaluate the effectiveness and clarify the working principles of the micro-ramp. The review paper from Lin<sup>2</sup> summarized the applications of micro-ramps prior to the year 2002 and several other applications were later reported.<sup>3-6</sup> Although its overall effectiveness is demonstrated through those studies, the detailed fluid physics of the micro-ramp is not yet fully understood.

Convinced by the successful implementation of micro-ramps in a large body of applications, Anderson *et al.*<sup>7</sup> and Hirt and Anderson<sup>8</sup> performed optimization investigations of micro-ramp

---

<sup>a)</sup>Electronic mail: [z.sun@tudelft.nl](mailto:z.sun@tudelft.nl).

arrays. In the computational study of Anderson *et al.*, several geometrical parameters including micro-ramp height ( $h$ ), chord length ( $c$ ), element spacing ( $s$ ), the distance between the micro-ramp and interaction region ( $x_p$ ), and the number of elements ( $n$ ) were considered as inputs. The response parameters were total pressure change across the SWBLI ( $\Delta P/P_0$ ) and transformed shape factor ( $H_{tr}$ ). The response surface method (RSM) was used to determine the optimal design, but  $H_{tr}$  is not minimized in the design space as  $\Delta P/P_0$  is maximized. In the study of Hirt *et al.*, only  $h$ ,  $c$ , and  $s$  were taken as inputs, while the boundary layer thickness  $\delta$  and the incompressible shape factor  $H_{inc}$  were chosen as response parameters. The RSM result showed that  $H_{inc}$  can be decreased at the cost of increasing  $\delta$ . Therefore, optimization for one parameter is at detriment of the other which requires trade-off consideration.

Based on the shape of the micro-ramp suggested by Anderson *et al.*,<sup>7</sup> several detailed studies on the effects of micro-ramp towards SWBLI were carried out experimentally and numerically. Herges *et al.*<sup>9</sup> visualized the flow fields before and behind the interaction region using particle image velocimetry (PIV) in five planes at different spanwise locations. A wake region with  $u$  deficit developing behind the trailing edge was revealed within the cross-flow planes ( $y$ - $z$  planes). This wake region structure was later confirmed by the numerical studies of Lee *et al.*<sup>10</sup> and Li and Liu<sup>11</sup> using monotone integrated large eddy simulation (MILES), through which the instantaneous properties of the wake could be studied. Notwithstanding the geometrical symmetry of the element, the instantaneous wake is not symmetrical to the center plane, with the primary counter-rotating vortex pair that is located inside the wake displaying a meandering behavior. A few other effects related to the Mach number,<sup>12</sup> geometry variations of the micro-ramp,<sup>13</sup> and declining angle of the trailing edge<sup>14</sup> were given specific attention as well.

Some detailed investigations on the micro-ramp flow upstream of the interaction region were also carried out in order to understand the fundamental aspects of the flow generated by a single micro-ramp. Babinsky *et al.*<sup>15</sup> inferred the flow topology from oil flow visualizations, and a model describing the streamwise vortices organization was formulated. According to Babinsky's description, a primary counter-rotating vortex pair and several secondary vortices emanate from the micro-ramp. The primary vortex pair is dominating the streamwise flow and is considered to play the major role in the boundary layer control. The downwash motion induced on the sides of the vortex pair transports high momentum fluids towards the wall, which results in a stronger capability of enduring the adverse pressure gradient across shock waves.

Blinde *et al.*<sup>16</sup> studied experimentally the micro-ramp flow in a supersonic boundary layer with stereo-PIV in planes parallel to the wall both in the inner and outer region of the boundary layer. Wall-normal vortex pairs were observed in the instantaneous visualizations of the wake, which were interpreted as the cross sections of the legs of hairpin vortices. A flow model of a train of hairpins, similar to those naturally occurring on top of low-speed flow regions inside a turbulent boundary layer, developing downstream of the micro-ramp was thus conjectured.

The numerical study by Li and Liu<sup>11</sup> visualized a train of vortex rings produced by Kelvin-Helmholtz (K-H) instability. Therefore, the organization of the flow only in part agrees with the model deduced from the experiment of Blinde *et al.*,<sup>16</sup> in particular, the legs of vortices do not appear to align with the floor like hairpins as proposed by Blinde *et al.* Instead, they rather appear to have a ring shape belonging to a plane that is only slightly inclined to the wall-normal direction. The ring vortices were proposed as a new working principle for the control of SWBLI, although their role in preventing boundary layer separation has not been fully explained.

The vortex-dominated structure of the upper part of the wake has been confirmed also by laser sheet visualization performed by Lu *et al.*,<sup>17</sup> where the seeded-unseeded interface pattern revealed K-H structures developing downstream of the micro-ramp. According to the explanation by Lu *et al.*, the K-H instability structures would develop as a secondary instability of the streamwise vortex pair, which is more stable in the region close to the micro-ramp and breaks down downstream into the roller structures at the interface. The process is regarded to be highly intermittent because of the local destabilization of the vortex pair. This latter model is in contrast with the previous two where no mention is made of the interaction between the streamwise vortices and the hairpin- or ring-shaped vortices.

Similar features have been observed in the flow around comparable structural elements, such as the mixing tab. This device is applied as a mixing device to strengthen momentum and heat exchanges, although it is larger in size and is typically used in the low-speed flow regime. The top surface of a mixing tab also features a contraction like a micro-ramp to induce the formation of a streamwise vorticity, and the resulting flow past both elements is therefore expected to present a similar organization. A conceptual model formulated by Greta and Smith<sup>18</sup> illustrates the instantaneous vortex structure containing the streamwise vortex pair wrapped up by hairpin vortices. Therefore, the hairpins generated by the mixing tab have a similar appearance to those proposed by Blinde *et al.*,<sup>16</sup> whereas this model containing two types of vortices simultaneously contradicts that proposed by Lu *et al.*<sup>17</sup> A following experimental research on the mixing tab by Yang *et al.*<sup>19</sup> using PIV visualized cross sections of heads and legs of the hairpins. Another important conclusion regarding the lifetime of the vortices in the resulting flow was reached: in the wake close to the mixing tab, the streamwise vortices are strong, however, they vanish after only 1.5 to 2.0 tab heights, depending on the Reynolds number. The flow is afterwards dominated by the hairpins, which can still be observed at  $\sim 12$  tab heights downstream. Although the persistence of the streamwise vortex pair is not clearly mentioned in the studies on micro-ramps, vortex rings visualized by Li and Liu<sup>11</sup> were still visible even after the interaction regions.

The questions emerging from the review of current work on the flow past micro-ramps are first the interaction between the supposedly steady streamwise vortex pair and the K-H vortices present at the wake interface. Moreover, the structure of the turbulent fluctuations downstream of the micro-ramp needs to be characterized statistically if any comparison is to be attempted between different experiments and computer simulations. Given the three-dimensional nature of the problem and the need to characterize the unsteady large-scale flow organization, three-dimensional measurements are performed in this study by the use of tomographic PIV (Elsinga *et al.*<sup>20</sup>). This technique has already been proven successful for the study of supersonic boundary layer turbulence by Elsinga *et al.*<sup>21</sup> and shock wave/turbulent boundary layer interactions by Humble *et al.*<sup>22</sup> and as such it is considered at a stage of sufficient maturity to measure the three-dimensional flow past a micro-ramp under the considered flow conditions.

The presentation of the results focuses first on the statistical characterization of the 3D wake, which is dominated by the primary streamwise vortex pair. The instantaneous large-scale organization is deduced by a vortex detection criterion in order to quantify the strength, occurrence, and length scales of K-H vortices. The relation between the streamwise vortices and the K-H vortices is revealed by means of three-dimensional instantaneous vorticity visualization. The discussion leads to a vortical model of the instantaneous vortex organization by conditional average process of the instantaneous flow fields.

## II. EXPERIMENTAL SETUP AND MEASUREMENT TECHNIQUE

### A. Flow facility and inflow conditions

Experiments were carried out in the blow-down supersonic wind tunnel ST-15 in the Aerodynamics Laboratory of Delft University of Technology. The wind tunnel has a test section of  $150 \times 150 \text{ mm}^2$  and was operated at Mach 2.0 with a total pressure  $p_0 = 3.2$  bars. The micro-ramp was installed on the wind tunnel bottom wall, where a turbulent boundary layer developed to a thickness of 6.0 mm.

Dedicated planar PIV measurements were carried out to characterize the properties of the undisturbed turbulent boundary layer. The digital resolution of the measurements is 81.1 pixel/mm, and the laser pulse time separation is set to  $\Delta t = 0.6 \mu\text{s}$  such that the free stream particle displacement is equal to  $300 \mu\text{m}$  (36 pixels). The boundary layer develops along a smooth surface under nearly adiabatic surface conditions for a length of  $\sim 1$  m and reaches a thickness  $\delta_{99} = 6.0$  mm, an incompressible displacement thickness  $\delta^* = 0.65$  mm, and an incompressible momentum thickness  $\theta = 0.54$  mm (incompressible shape factor  $H_{inc} = 1.20$ ). Using the van Driest II transformation in combination with the Crocco-Busemann relation and a recovery factor  $r = 0.89$ , a skin friction coefficient  $c_f = 2.6 \times 10^{-3}$  was determined, corresponding to a friction velocity  $u_\tau = 19.0$  m/s.

TABLE I. Experimental conditions and undisturbed boundary layer conditions.

Parameter	Quantity
$Ma_\infty$	2.0
$u_\infty$ (m/s)	534
$P_0$ (Pa)	$3.2 \times 10^5$
$T_0$ (K)	290
$\delta_{99}$ (mm)	6.0
$\delta^*$ (mm)	0.65
$\theta$ (mm)	0.54
$H_{inc}$	1.20
$u_\tau$ (m/s)	19.0
$C_f$	$2.6 \times 10^{-3}$
$Re_h$	140 000
$Re_\theta$	15 740

The Reynolds number based on the micro-ramp height is  $Re_h = 140\,000$ , and the Reynolds number based on the incompressible momentum thickness is  $Re_\theta = 15\,740$ . The experimental conditions and undisturbed turbulent boundary layer parameters are summarized in Table I. It should be noted that the free stream velocity  $U_\infty$  is used as a reference velocity for normalization and labeled as  $U_{ref}$ .

The boundary layer profile including the log law fit is shown in Figure 1. The resolved log region of the boundary layer approximately covers the range of  $900 < y^+ < 3000$ , which corresponds to  $0.06 < y/\delta_{99} < 0.4$ . The measurement point closest to the wall corresponds to  $y^+ = 700$ , but already deviates from the log fit, as a result of the resolution limits of the current PIV experiment. Beyond the log region, the wake component is retrieved in the range  $y^+ > 3000$ .

The wall-normal profiles of the turbulent fluctuations in the undisturbed boundary are shown in Figure 2, where the PIV results from Humble *et al.*<sup>22</sup> and the incompressible flow data from Klebanoff are included for comparison. The root mean square (RMS) velocity components are normalized by the friction velocity, and the density variation is taken into account by multiplying by the density ratio  $\sqrt{\rho/\rho_w}$  according to Morkovin's hypothesis, so that the incompressible data of Klebanoff can be compared to the compressible flow results.

The fluctuations of the streamwise velocity component agree well with the result from Humble, considering that the experiments were conducted in different wind tunnels, except at the region close to the wall. Both experiments yield higher values of  $\langle u' \rangle$  compared to the Klebanoff data. The opposite occurs for the wall-normal fluctuations, where the current experiments also yield lower values of  $\langle v' \rangle$ . These discrepancies may reflect the velocity measurement uncertainty, but may also partly be attributed to the limited validity of the density-weighted scaling of, in particular, the wall-normal component of the velocity.

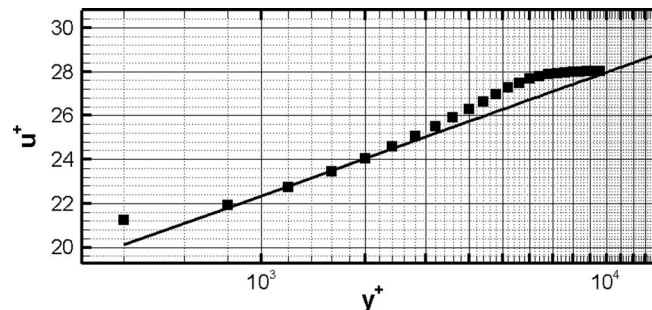


FIG. 1. Log law fit of undisturbed boundary layer profile.

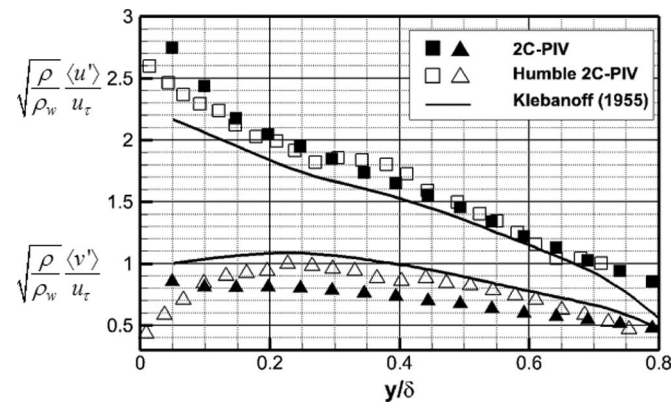


FIG. 2. Velocity fluctuations in the undisturbed boundary layer.

### B. Micro-ramp configuration

A single micro-ramp with a height  $h = 4$  mm was investigated in the present experiment. The geometry follows from the optimization study performed by Anderson *et al.*<sup>7</sup> resulting in a chord length of  $c = 27.4$  mm and a spanwise width of  $w = 24.4$  mm (see Figure 3). In Figure 4 a schematic representation of the experimental setup is shown with the micro-ramp mounted on the wind tunnel bottom wall. Note that the micro-ramp and the laser volume are exaggerated for clarity.

### C. Tomographic particle image velocimetry

Tomographic particle image velocimetry (Tomo-PIV) is a 3D velocimetry technique based on the principles of optical tomography. Several cameras observe the illuminated region (typically taking the form of a thick sheet of light) from non-collinear viewing directions. The number of cameras required for a tomographic experiment depends amongst others upon the concentration of tracer particles present in the measurement domain. Typically, three to six independent viewing directions are required.<sup>20</sup> The present Tomo-PIV setup makes use of three cameras as shown in Figure 4, of which one was placed with a viewing axis normal to the illumination median plane. The other two were placed upstream in order to collect light scattered by the particles in the forward direction, which gives a significant benefit in terms of detected particle signal.

The flow was seeded with di-ethyl-hexyl-sebacate (DEHS) with a nominal diameter of  $\sim 1$   $\mu\text{m}$ . The particles were injected into the flow before entering the settling chamber. According to experiments performed by Ragni *et al.*,<sup>24</sup> the DEHS particle tracers have a relaxation time of  $\sim 2$   $\mu\text{s}$  in a Mach 2 flow. Due to the presence of the mesh screens inside the settling chamber and the turbulence in the boundary layer, the particle tracers are mixed uniformly in the flow, resulting in a homogenous particle distribution in the measurement domain. The particle tracers were illuminated by a spectra-physics quanta ray double-pulsed Nd:Yag laser with 400 mJ pulse energy and a 6 ns

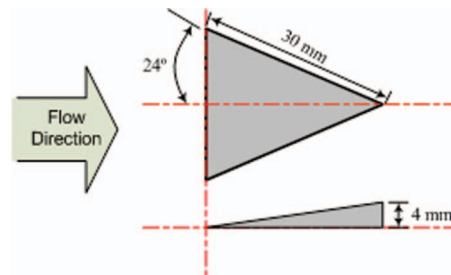


FIG. 3. Dimensions of the micro-ramp.

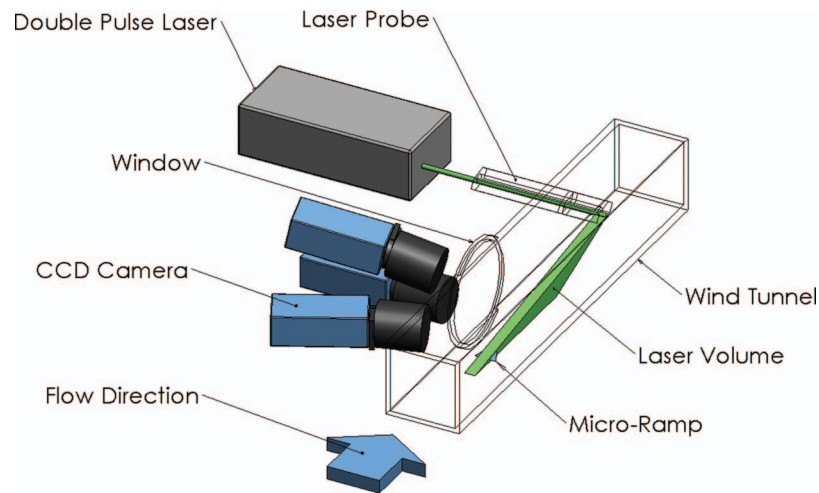


FIG. 4. The Tomo-PIV experimental setup, the micro-ramp, and the laser volume are exaggerated for clarity.

pulse duration at a wavelength of 532 nm. The laser beam was shaped into a volume with main dimensions along the streamwise and wall-normal directions and a thickness of  $\sim 6$  mm along the span. The laser light volume was formed through a periscope probe, which was designed to withstand the supersonic flow conditions and positioned downstream of the test section.

The particle images were recorded by three PCO Sensicam QE cameras having Peltier-cooled CCD sensors with  $1376 \times 1040$  pixels and 12 bits quantization. The active sensor region was cropped along the vertical direction where 896 pixels were used given the aspect ratio of the region of interest. The acquisition frequency of the system was 5 Hz. Each measurement comprised 400 triplets of image pairs to allow statistical analysis of the turbulent flow properties. The flow was imaged in the streamwise ( $x$ ), wall-normal ( $y$ ), and spanwise ( $z$ ) directions over a volume of  $\sim 25 \times 15 \times 6$  mm<sup>3</sup>, respectively, with an average digital image resolution of 43.7 pixels/mm. Each camera was equipped with a Nikon 105 mm focal length objective. Camera-lens tilt adapters were attached to guarantee the Scheimpflug condition between the image plane and the illuminated median plane. The two cameras in forward scattering were set to  $f_{\#} = 16$ , and the camera normal to the measurement volume was set to  $f_{\#} = 11$ . The Tomo-PIV recording parameters are summarized in Table II.

The achievable measurement volume depth is limited by the available energy of the light source, and the Tomo-PIV measurement domain spans 6 mm, which is about 1/4 of the width of the micro-ramp. However, the hairpins have a size that is approximately half of the width of the micro-ramp in the spanwise direction.<sup>16</sup> Therefore, two measurements were carried out with different positions of the laser volume (see Figure 5). For the configuration indicated as Measurement I, the laser volume is centered on the symmetry plane of the micro-ramp. In the second configuration (Measurement II), the edge of the volume was aligned with the micro-ramp symmetry plane. Both measurement

TABLE II. Tomographic PIV recording parameters.

Parameter	Quantity
Measurement volume	$25 \times 15 \times 6$ mm <sup>3</sup>
Interrogation volume	$1.46 \times 1.46 \times 1.46$ mm <sup>3</sup>
Digital imaging resolution	43.7 pixels/mm
Object focal length	$f = 105$ mm
$f$ -number	$f_{\#} = 11, 16$
Laser pulse separation	$0.6$ $\mu$ s
Seeding density	0.05 particle/pixel

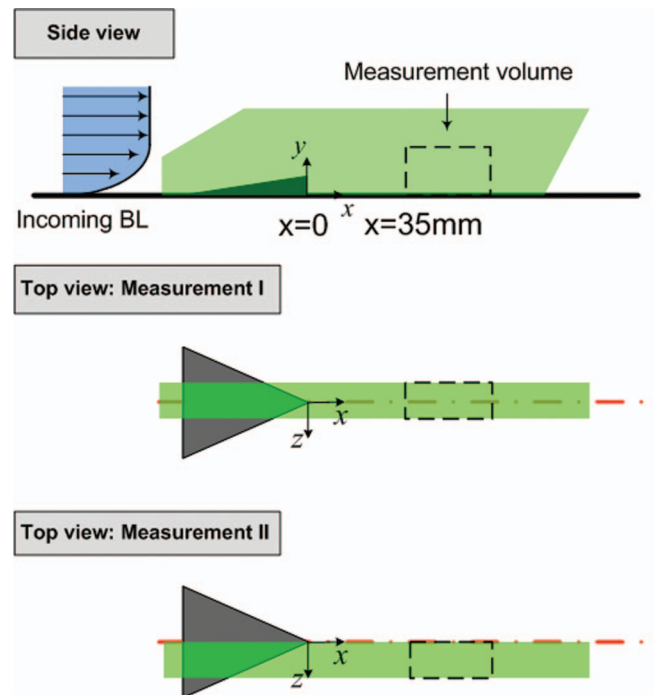


FIG. 5. Schematic of the micro-ramp with coordinate system and laser volume position.

volumes are located 35 mm ( $8.75h$ ) downstream of the trailing edge in order to avoid reflections coming from the micro-ramp. This results in a measurement range extending from  $x/h = 8.75$  to 15 in streamwise direction. The definition of the coordinate system is indicated in Figure 5, with the origin of the coordinate system placed at the trailing edge of the micro-ramp.

The DAVIS 7.4 software package was used for data acquisition and processing (volume calibration, self-calibration, image preprocessing, reconstruction, and three-dimensional cross-correlation). The volume calibration was performed using three parallel planes located at equal intervals of 3 mm. The particle images were preprocessed by subtracting the time-minimum pixel intensity to reduce the overall background intensity. Furthermore, Gaussian smoothing with a  $3 \times 3$  kernel was applied to reduce image noise. The particle images were interrogated using volumes with final size of  $64 \times 64 \times 64$  voxels and an overlap factor of 50%. Spurious vectors were removed and replaced through linear interpolation of surrounding vectors. Due to laser light reflections, the region close to the wall could not be accessed and was therefore excluded from the analysis. For this reason the measurement volume starts from  $y = 2.52$  mm ( $0.63h$ ) in wall-normal direction.

It may be mentioned that the dataset of 400 snapshots for each measurement is the result of 8 runs of the wind tunnel. This arrangement was adopted in view of the progressive contamination of the laser probe window as a result of the deposit of the DEHS seeding for a prolonged wind tunnel run time. Each wind tunnel operation had a total run time of 15 s including the starting time of  $\sim 5$  s. The temperature drop rate of the wind tunnel is  $\sim 0.1$  K/s. Then the temperature drop for each run of the wind tunnel is about 1 K, which is deemed to have a negligible effect on the velocity measurement within the experimental uncertainty.

#### D. Uncertainty analysis

The experimental uncertainty is dominated by that of the PIV measurement technique in the present investigation. Several factors can be discerned that affect the measurement uncertainty; the most important ones are the finite data ensemble size, the cross-correlation algorithm, and the limited particle tracer response.

Based on the ensemble of  $N = 400$  uncorrelated velocity fields produced in the Tomo-PIV measurement, the statistical component of velocity uncertainty is estimated to be  $0.8\% U_{ref}$  inside

TABLE III. Uncertainty parameters.

Parameter	Planar PIV ( $N = 200$ )	Tomo-PIV ( $N = 400$ )
Statistical uncertainty $\varepsilon_{\bar{u}}/U_{ref}$	0.71%	0.8%
Cross-correlation uncertainty $\varepsilon_{cc}$	0.1 pixels	0.2 voxels
Instantaneous velocity $\varepsilon_{u(\varepsilon_{cc})}/U_{ref}$	0.3%	0.5%
Velocity fluctuations $\varepsilon_{\langle u' \rangle} / \langle u' \rangle_{max}$	2%	5%
Reynolds shear stress $\varepsilon_{\overline{u'v'}} / (\overline{u'v'})_{max}$	20%	50% (wake region)
Spatial resolution effect $\varepsilon_{(WS/\lambda)}/U_{ref}$	1%	2%–10%
Particle slip $\varepsilon_{\tau_p}/U_{ref}$	$\leq 2\%$	$\leq 2\%$
$\varepsilon_{\omega}/\omega_{max}$	...	$\sim 20\%$ – $30\%$

the wake region, where the largest velocity fluctuations occur. Correspondingly, the uncertainty of  $\langle u' \rangle$  and  $\overline{u'v'}$  are estimated to be  $5\% \langle u' \rangle_{max}$  and  $50\% (\overline{u'v'})_{max}$  in the wake region, respectively.

The cross-correlation of the digital particle images also produces random uncertainty onto the measured instantaneous velocity field. A value of 0.2 voxels is conservatively assumed for the present Tomo-PIV,<sup>23</sup> which corresponds to  $\sim 0.5\%$  of the free stream velocity.

The PIV measurements are conducted at finite spatial resolution. The measurement element is a cube of  $1.46^3 \text{ mm}^3$  and velocity vectors are placed at discrete locations separated by  $\sim 0.73 \text{ mm}$ . Spatial fluctuations of length scale comparable to that of the interrogation element lead to errors due to the filtering effect of the spatial cross-correlation.<sup>25</sup> Considering the wavelength of the Kelvin-Helmholtz vortices, the uncertainty due to finite spatial resolution is estimated between 2% and  $10\% U_{ref}$ .

Another effect that needs to be taken into account is the tracer particle fidelity which is quantified by the particle response time  $\tau_p$ . The amount of particle slip is estimated by multiplying the particle response time  $\tau_p$  ( $\tau_p \approx 1.92 \mu\text{s}$  for DEHS (Ref. 24)) with a relevant particle acceleration  $a_p$ . In the current work the most relevant acceleration is related to the vortical motions in the flow (either in streamwise or cross-flow direction), for which the centrifugal acceleration is estimated to be  $5.28 \times 10^6 \text{ m s}^{-2}$ , this results in an uncertainty of  $\sim 2\% U_{ref}$ .

As the present work focuses on the vortical structures as a flowfield property of interest, an uncertainty estimate for vorticity is essential. The vorticity is calculated by spatial central difference. Based on error propagation theory and neglecting the uncertainty on the window spacing, the precision error for the vorticity can be estimated through the expression:

$$\varepsilon_{\omega_z} = \frac{\varepsilon_u}{4\sqrt{2}h}, \quad (1)$$

where the denominator indicates the averaging of the two velocity components by the coefficient  $\sqrt{2}$ . The factor 4 is the result of twice the vector spacing (finite differences) and the interrogation window overlap factor. As a result, the random error on the vorticity is  $\sim 10\% \omega_{max}$ . The peak vorticity is systematically underestimated due to finite resolution as also discussed for the velocity. The typical error associated to signal modulation takes into account the interrogation block size, the kernel used for finite differences, and a post-processing operation that applies a Gaussian filter to the vorticity field. The estimated error on the peak values is between 20% and 30% of the maximum vorticity. The uncertainty parameters are summarized in Table III.

### III. MEAN FLOW ORGANIZATION

The organization of the mean flow is first addressed to provide the basic flow topology as a framework for the subsequent discussion of the more complex flow features that occur in the instantaneous flow. The mean flow field is obtained by averaging the three-dimensional data fields throughout the entire dataset, and it is represented in Figure 6 through three cross-flow slices at streamwise locations of  $x/h = 8.75, 11.25, 13.75$  (i.e.,  $x = 35 \text{ mm}, 45 \text{ mm},$  and  $55 \text{ mm}$ ) and one  $x$ - $y$  cross section at the median plane ( $z/h = 0$ ). The cross sections in Figure 6 represent the streamwise

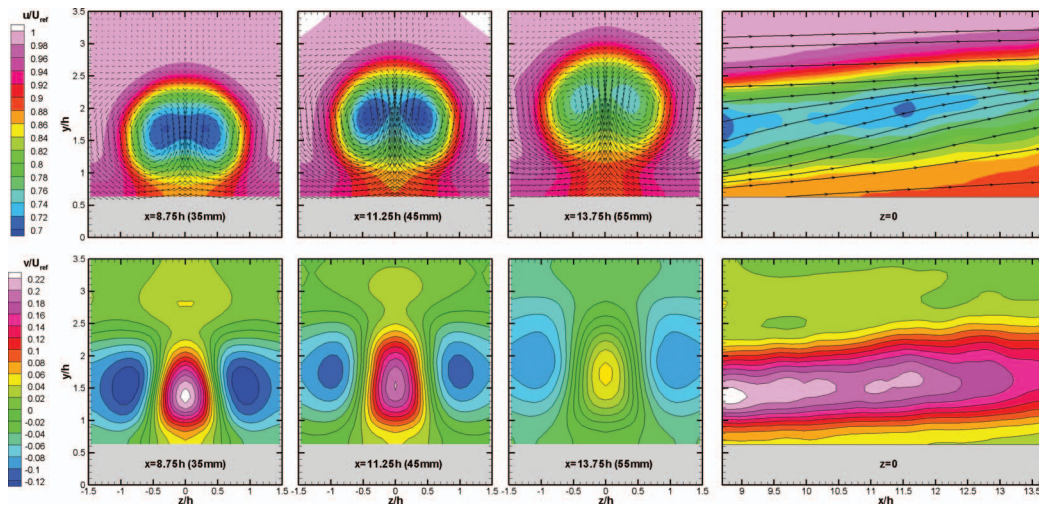


FIG. 6. Selected two-dimensional cross sections of  $u$  and  $v$  contours of the mean flow field, cross-flow vectors, and streamlines in the median plane have been added to the  $u$  contours.

(top) and wall-normal (bottom) velocity distributions, respectively. For ease of interpretation, the velocity field is mirrored around the median plane in the assumption of a symmetrical mean flow field. This assumption has been verified by means of planar measurements along the entire span of the ramp, which confirmed a high degree of symmetry of the mean flow.

The streamwise vortex pair is presented as the major flow feature in most studies and will be addressed first. This pair of vortices can be observed through the projected vectors in the first three  $y$ - $z$  plane plots in Figure 6. At the upstream position ( $x = 8.75h$ ), the vertical position of the vortex core is approximately at  $y = 1.63h$ , and the separation between the two vortices axes is of the size of  $h$ . With increasing distance downstream, the vortex system moves up in height at an approximately linear rate: at  $x = 13.75h$  the height of the vortex is at  $y = 2.13h$ . In contrast, the spanwise extent appears relatively unchanged, and the distance between the vortices stays almost the same as in the upstream locations. The streamlines inside the wake region exhibit a typical S-shape at the wake symmetry plane ( $z/h = 0$ ), indicating the upwash flow induced by the vortex pair.

According to the  $u$  contours in Figure 6, the wake appears as a region with a rather circular cross section featuring two counter-rotating streamwise vortices and bounded by the shear layer at the outer edge. Each vortex is accompanied by a momentum deficit attaining a maximum slightly inside and above the position of the vortex core. The upward shift of the overall wake can be explained by considering that the vortex pair system is subject to a net positive lift force.

The vertical velocity contours show a vigorous upwash at the symmetry plane attaining a velocity above  $0.2U_{ref}$ . The downwash regions extend over a large area with approximately half the intensity.

The properties of the shear layer are explored through the velocity profiles in Figures 7 and 8. The three  $u$  profiles shown in Figure 7 belong to different streamwise positions of  $x/h = 8.75$ , 11.25, and 13.75 which represent different stages of wake development in the current measurement domain. Their wall-normal positions correspond to that of the vortex.

The three profiles are all basin-shaped with  $u$  deficit at the center. The minimum value of the streamwise velocity component is  $0.7U_{ref}$  at  $x/h = 8.75$ . Further away from the centerline the streamwise velocity will increase to reach the free stream magnitude within a spanwise distance of  $\Delta z \approx 1.125h$ . The latter can be regarded as the wake semi-width. When the wake develops downstream, the recovery process reduces the momentum deficit.

On its lower side, the wake flow is affected by the presence of the wall, where the non-slip condition is applied. The bottom part of the wake consequently exhibits different properties compared to the top part which is bordering on the free stream. Figure 8 shows six wall-normal profiles of the streamwise velocity that have been extracted at the same streamwise position of  $x/h = 8.75$ , for

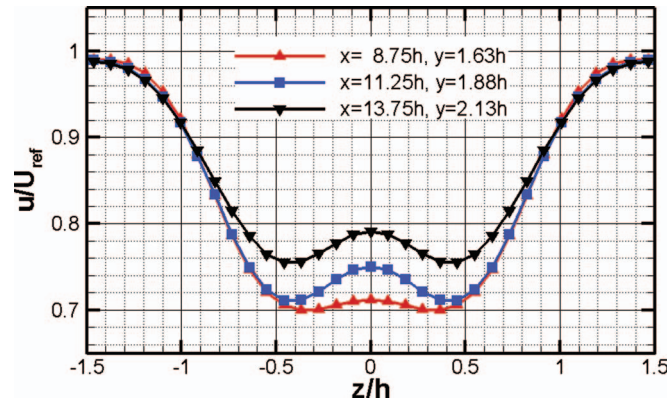


FIG. 7. Spanwise distributions of the streamwise velocity component, profiles are taken at the height of the vortex cores.

different spanwise positions, varying from the center ( $z/h = 0$ ) to outside the wake ( $z/h = 1.5$ ). The undisturbed boundary layer is also included to illustrate the possible advantage of the micro-ramp in boundary layer control. Two shear layer regions can be distinguished. The upper shear layer of the profile at the center plane ( $z/h = 0$ ) is similar to the shear layer explained in Figure 7: the  $u$  increases from the minimum deficit to the free stream magnitude also within a comparable thickness of  $\Delta y \approx 1.13h$ . However, the lower shear layer presents different features, as it is embedded in the plate boundary layer. The  $u$  increases to a magnitude less than the free stream value, for example, the center profile at  $x/h = 8.75$  increases to  $0.87U_{ref}$ .

As addressed in the literature, the energized boundary layer is achieved through the downwash motion. The  $v$  contours in Figure 6 clearly visualize the upwash and downwash regions. A more detailed analysis is offered in Figure 9, where spanwise profiles are extracted at the vortex core location. The upwash has a maximum of  $0.2U_{ref}$  at  $x/h = 8.75$ , while the downwash obtains a magnitude of  $-0.14U_{ref}$ . The wake growth caused by the recovery reduces the amplitude of wall-normal motion and at  $x/h = 13.75$  the upwash and downwash have been reduced to  $0.14U_{ref}$  and  $-0.8U_{ref}$ , respectively.

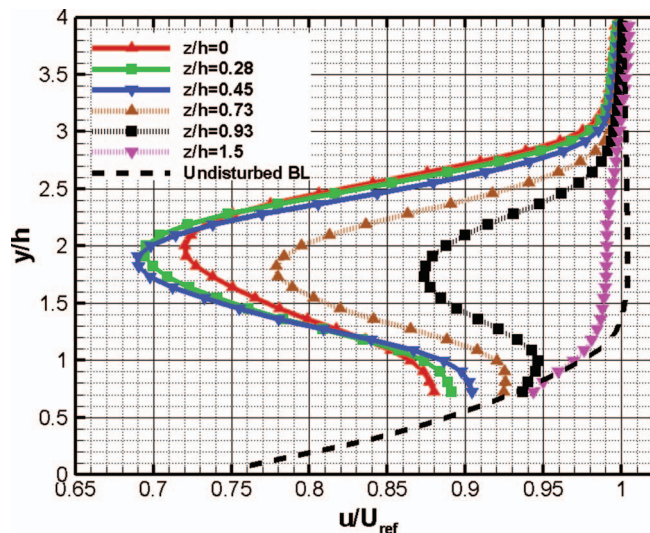


FIG. 8. Wall-normal distribution of the streamwise velocity component at  $x/h = 8.75$ . Profiles are shown for a varying spanwise distance from the wake symmetry plane.

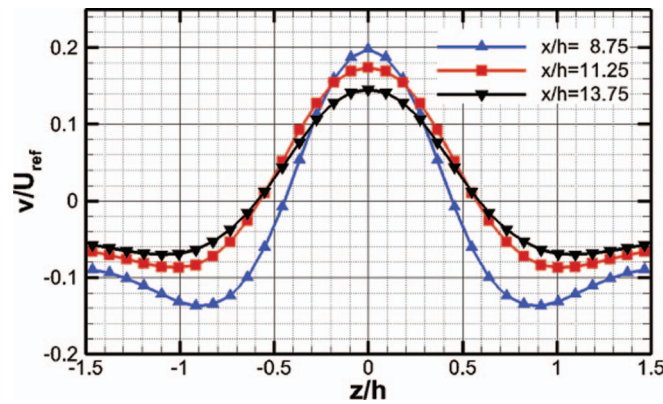


FIG. 9. Spanwise distributions of wall-normal velocity component at three streamwise positions.

#### IV. INSTANTANEOUS FLOW ORGANIZATION

In this section, the analysis focuses on the instantaneous velocity pattern, and the vortical structure is later elaborated upon. Furthermore, the interaction between the two categories of vortices that are observed in the flow field, namely, the primary streamwise vortices and the K-H vortices, is investigated.

##### A. Instantaneous velocity structures

For ease of interpretation, the discussion of the instantaneous three-dimensional velocity structure will initially be approached through the observation of flow patterns in the cross-sectional planes. The volumetric representations of the velocity field are then subsequently presented to provide a global view of these patterns in three-dimensions.

Figure 10 illustrates the instantaneous flow field through four  $y$ - $z$  cross-sectional representations at the same streamwise position of  $x/h = 10.5$ , corresponding to four snapshots that are uncorrelated in time (the time separation is more than 1 s). The vortex pair is seen to exhibit significant variations in its spanwise position. Moreover, the vortices can appear profoundly distorted with respect to the time-averaged flow field presented before. Nevertheless, the basic structure with a pair of counter-rotating vortices is maintained and the momentum deficit concentrated at the vortex cores is observed in most of the realizations.

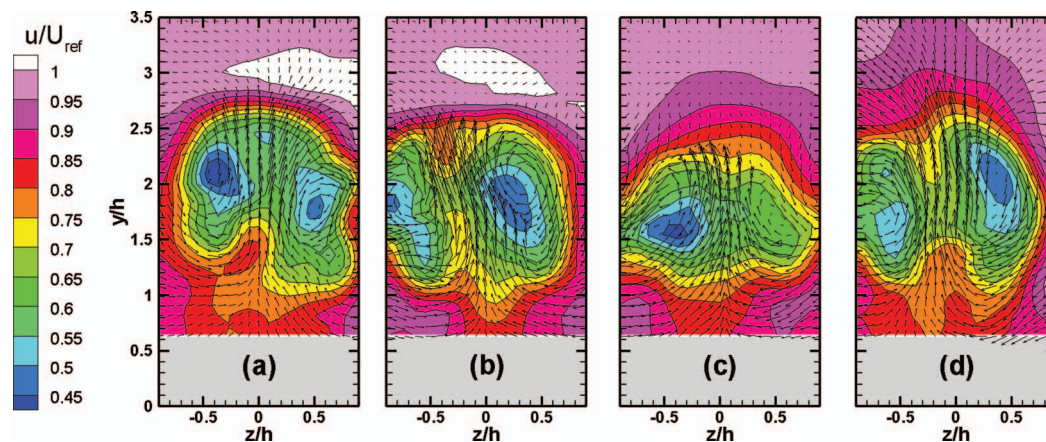


FIG. 10. Contours of  $u$  in four instantaneous  $y$ - $z$  planes at fixed streamwise position of  $x/h = 10.5$ . Vectors represent only the in-plane velocity components.

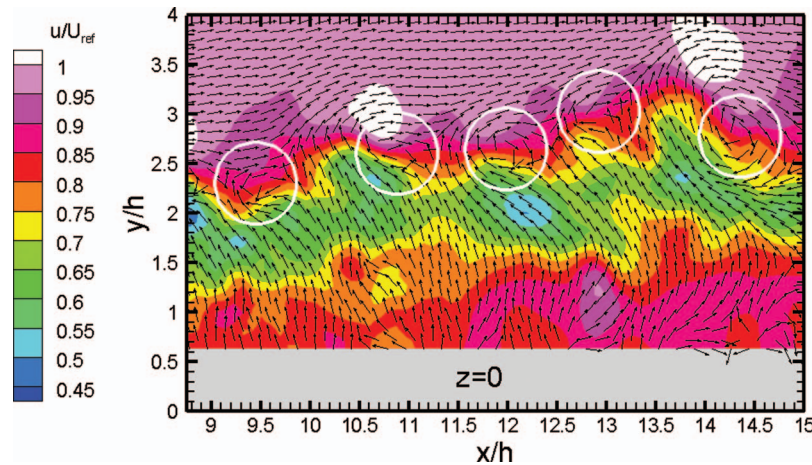


FIG. 11. Contours of  $u$  in the median plane ( $z/h = 0$ ). Velocity vectors are represented in a convective frame of reference ( $U_{conv} = 0.88U_{ref}$ ) to visualize the K-H vortices in the shear layer (indicated by white cycles).

The vortex pair is no longer symmetric along the median plane at  $z/h = 0$ , and the edge of the wake region is not as regular as in the mean flow. A significant difference can be observed in the first two plots of Figure 10, where a high-velocity pocket is generated above the wake region. This distinctive flow feature can be explained through the longitudinal  $x$ - $y$  cross section along the median plane, as shown in Figure 11 (the cross sections in Figures 11 and 10(a) are extracted from the same snapshot).

The instantaneous representation of  $u$  in the streamwise-wall-normal plane exhibits large-scale fluctuations at the interface between the wake region and the free stream. This wavy structure can be recognized as the imprint of a K-H instability. This is reflected by the rather regular formation of spanwise vortices rotating in the same direction as the mean shear. The vortices typically travel at a convective velocity of  $0.83U_{ref}$ . When represented in a convective frame of reference, the velocity vector pattern will reveal the typical swirling motion with clockwise rotation. The fluid above the vortex is locally accelerated, while accordingly, the flow below is decelerated.

A volumetric representation is employed to further illustrate the velocity pattern in a three-dimensional way. This is performed by selecting three values of the  $u$  that allow visualization of typical flow field features by the iso-surfaces plotted in Figure 12. It should be noted that the flow fields in Figures 12(a) and 12(b) are from Measurement I and they represent the same snapshot as Figure 11, while Figures 12(c) and 12(d) are from Measurement II. The local high-speed regions induced by the presence of the K-H vortices are shown in pink ( $u = 1.02U_{ref}$ ), while the low-speed regions ( $u = 0.8U_{ref}$ ) below the K-H vortices are shown in green. In Figure 12(a), it can be seen that the high-speed regions span the whole measurement volume, while they tend to bend towards the wall when moving further in spanwise direction (see Figure 12(c)). In combination, it can be concluded that the high-speed regions, hence, feature an arc-shaped form. For the low-speed regions depicted in green, the spanwise orientation is less pronounced although it is clear that they appear in combination with the high-speed regions confirming the presence of the K-H vortices.

Figures 12(c) and 12(d) show an iso-surface in yellow that represents an intermediate speed  $u = 0.9U_{ref}$  region in combination with the high-speed regions for reference. The velocity value for the yellow iso-surface is chosen such that it illustrates the extent of the shear layer and the wake in which the streamwise vortex pair is developing. As illustrated in Figure 6 the low-speed region forms a continuous, connected region in the mean flow representation. In the instantaneous flow, however, due to the local backward flow effect induced below the K-H vortices, the low-speed region develops into several packets as depicted in Figures 12(a) and 12(c).

Since the high-speed packets are the result of the K-H instability, the resulting vortices are expected to obtain a similar arc-like shape. This can be validated by visualizing the velocity field in the  $x$ - $z$  plane, see Figure 13. In order to visualize the imprints of the vortices, the  $u$  is plotted

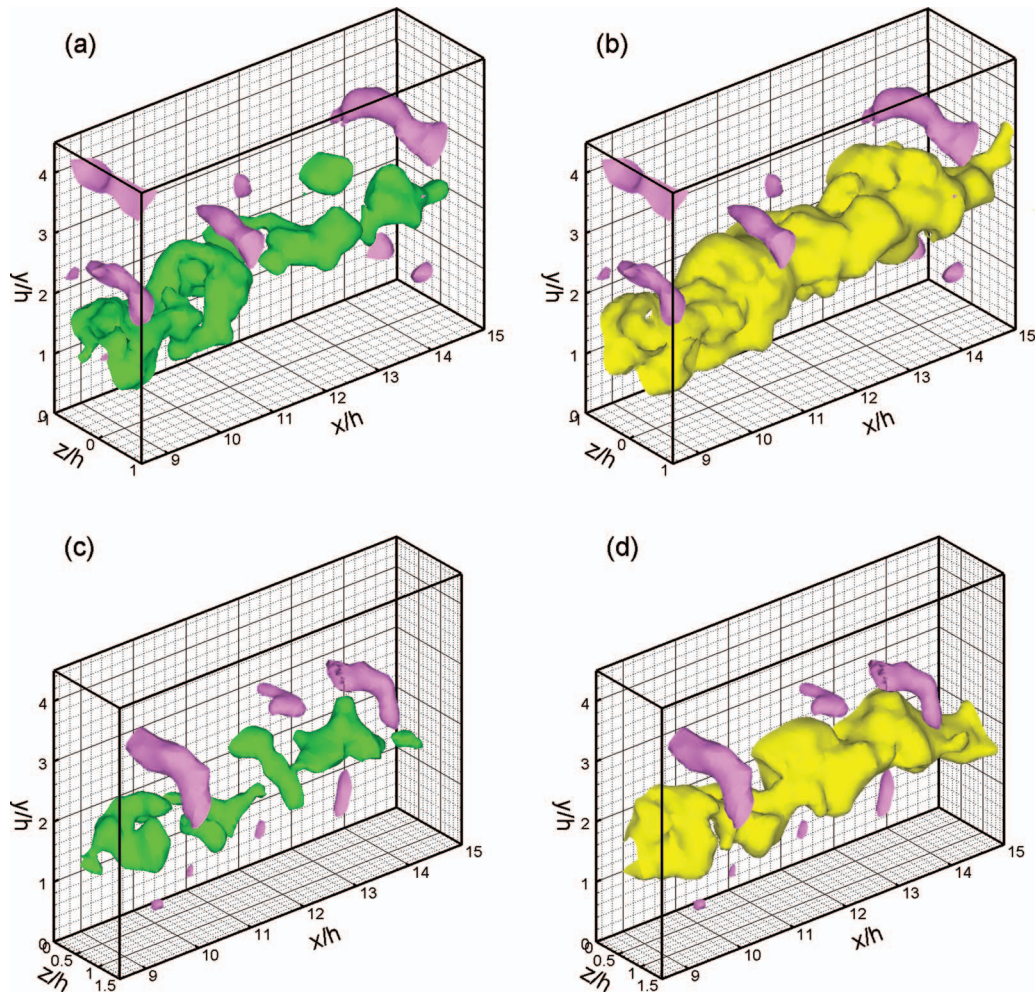


FIG. 12. Iso-surfaces of  $u$  in the domain of two measurements. The first row is from Measurement I and the second row is from Measurement II. Three values of  $u$  are chosen: high speed  $1.02U_{ref}$  (pink), intermediate  $0.9U_{ref}$  (yellow), and low speed  $0.8U_{ref}$  (green).

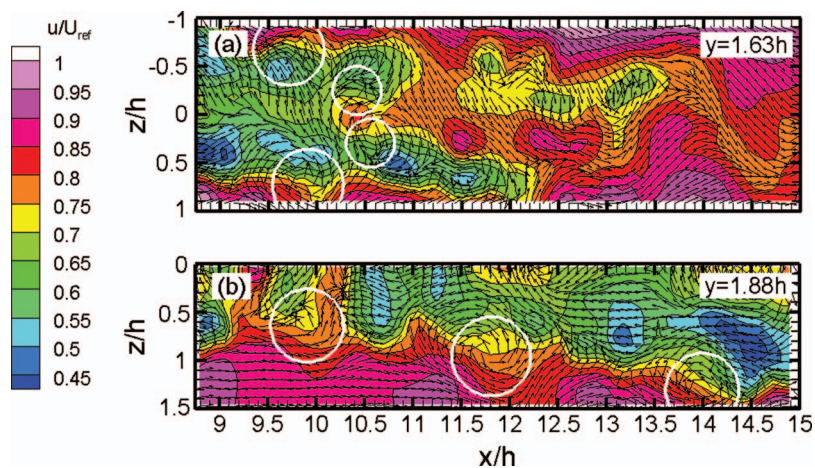


FIG. 13. Contours of  $u$  in the wall-parallel plane at different heights. Vectors are overlaid, and a constant value has also been subtracted from the original vector field to visualize the K-H vortices which are indicated by the white cycles. (a)  $x$ - $z$  plane at  $y/h = 1.63$  from a snapshot in Measurement I and (b)  $x$ - $z$  plane at  $y/h = 1.88$  from a snapshot in Measurement II.

in a convective frame of reference (similar to Figure 11). Figure 13(a) contains a snapshot from Measurement I and shows a pair of vortices at the edge of the wake region at  $x/h \approx 10$ . Because the wake expands when moving further downstream, the vortex pairs are beyond the measurement domain. The cross section in Figure 13(b) shows a snapshot taken from Measurement II, since this volume only contains one side of the flow field, only one vortex of each pair is visualized. Similar to what is observed in the center plane (Figure 11) K-H instability is observed in the shear layer at both sides of the wake. A series of vortices is indicated by the white circles that are located in the shear layer and represent the cross sections of the leg portions of the arc-shaped vortices.

Closer inspection of Figure 13(a) reveals a pair of secondary vortices with reversed rotation from their neighboring primary ones. The secondary vortices appear inside the wake region and the distance between them is much shorter,  $\sim 0.5h$  for current realization. Due to their rotations, the flow between them is ejected forward, generating a local high-speed region. According to the experimental study of Yang *et al.*,<sup>19</sup> similar pairs of secondary vortices were observed and they were further identified as the imprints of secondary hairpin vortices whose head cross sections could be observed in the wall-normal plane containing the streamwise direction. This category of secondary hairpins was later testified by the study of Dong and Meng<sup>26</sup> through direct numerical simulation. However, the cross section of the head part of the secondary hairpin cannot be observed in Figure 11. The reason could be that this secondary hairpin is rather weak and just appears as fragments.

So far, the instantaneous velocity patterns have been discussed and highly three-dimensional effects are observed. The visualization of the K-H instability confirms the computational results by means of LES of Li and Liu<sup>11</sup> and the qualitative experimental observations by Lu *et al.*<sup>27</sup>

## B. Coherent vortical structures

Studying the predominant coherent structures will aid in understanding the turbulent flow field generated by the micro-ramp and provides a first insight into its dynamics. The two most important vortical structures that are observed are the counter-rotating streamwise vortices and the K-H vortices in the shear layer. In order to fully understand the fluid physics of the micro-ramp, it is important to understand the interaction between these vortical structures.

In Figure 14(a), a snapshot of the streamwise vortices is shown by plotting the iso-surface of  $\omega_x$ , the different colors denote opposite signs of vorticity (positive in green and negative in pink). In Figure 14(b) the K-H vortices are shown in orange by plotting the iso-surfaces of the  $z$ -component of vorticity  $\omega_z$ . Recall that from the average flow field it seems that the streamwise vortices develop in a straight path, however, from the instantaneous realization it can be observed that they meander.

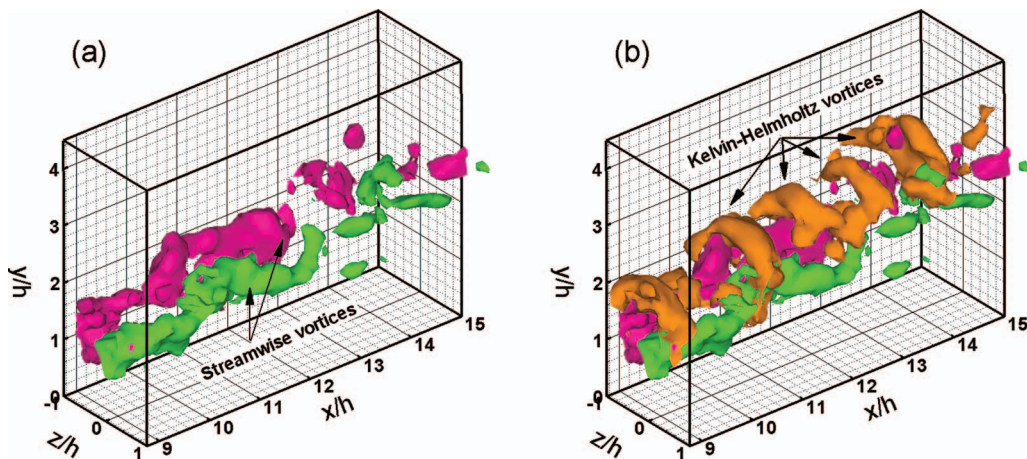


FIG. 14. Iso-surfaces of the vorticity from one snapshot. (a) Iso-surfaces of  $\omega_x$  and (b) iso-surfaces of  $\omega_z$  together with iso-surfaces of  $\omega_x$ .

At upstream locations ( $x/h < 12.5$ ), the vortex pair is well defined by the choice of the iso-surface value. Further downstream the iso-surface becomes fragmented which gives an indication that the vorticity magnitude becomes less due to diffusion. According to the experiments of Elavarasan and Meng on the mixing tab,<sup>28</sup> the streamwise vortices in the wake of a mixing tab typically last only 1.5 to 2.0 tab heights from the trailing edge. However, in the current research the vortices still exist even after 12.5 ramp heights. This large difference can possibly be attributed to different Reynolds number and Mach number: the mixing tab was installed in a low-speed water flow ( $Re_h = 700$ ), while the micro-ramp is implemented in a supersonic compressible flow ( $Re_h = 140\,000$ ).

Figure 14(b) clearly shows the head part of the arc-shaped K-H vortices; they are located directly over the streamwise vortices and span the entire width of the measurement domain. Upon close inspection it can be furthermore observed that the K-H vortices curve toward the wall when moving away from the micro-ramp centerline, effectively encompassing the top part of the streamwise vortices.

### C. Analysis of vorticity interaction

The interaction between the system of K-H vortices and the streamwise vortex pair is studied. The vorticity vector is decomposed along the streamwise and the spanwise directions. A surface integral of vorticity component is employed to quantify the strength of the vortical structures. The vorticity integral for each vortex is defined in the following way similar as Li *et al.*:<sup>29</sup>

$$F_{x+}(x) = \iint \omega_x^+ dydz, \quad (2)$$

$$F_{x-}(x) = \left| \iint \omega_x^- dydz \right|, \quad (3)$$

$$F_{z-}(x) = \left| \int \omega_z^- dy \right|, \quad (4)$$

where  $F_{x+}(x)$  is the surface integration of positive (clockwise rotating when viewed from upstream) streamwise vorticity ( $\omega_x^+ > 0$ ) at each cross-flow plane ( $y$ - $z$  plane). This operation is carried out by integrating the positive streamwise vorticity inside every cross-flow plane.  $F_{x-}(x)$  has a similar definition, but for the opposite rotating direction ( $\omega_x^- < 0$ ). The absolute value is considered for the latter since only the magnitude of the vorticity integral is of interest. The existence of a K-H roller is detected by a peak of  $F_{z-}(x)$ . To perform further operations, subtraction and amplitude normalization by the mean value is made.

The typical distributions of the vorticity integrals from one snapshot are shown in Figure 15. It should be noted that the negative peak of the normalized vorticity integral means a local minimum instead of a negative vorticity integral. The top view included in Figure 15 illustrates the three-dimensional pattern of the instantaneous vorticity to clarify the relation between the vorticity integrals and the spatial organization of the flow.

Not surprisingly,  $F_{z-}(x)$  exhibits the strongest fluctuations along the streamwise direction, which is associated to the presence of concentrated vorticity at the position of K-H rollers. The streamwise vortex pair, which has been often considered to develop smoothly along  $x$  (see, e.g., Babinsky *et al.*<sup>15</sup>), also shows visible fluctuations. Observing the diagrams, a phase relation between the K-H vortices ( $F_{z-}$ ) and the streamwise vortex pair ( $F_{x+}$  and  $F_{x-}$ ) can be hypothesized. Namely, the streamwise vorticity peaks are located slightly upstream of those from the spanwise component. A cross-correlation analysis performed on the entire data ensemble confirms a positive peak,  $\sim 0.5h$  or 2 mm, upstream and a negative one downstream with a similar distance, see Figure 16. The result is rather comparable for each of the two vortices from the streamwise pair. The negative peak corresponds to the position where the intensity of the streamwise vortex attains a minimum. Instead, the positive peak upstream indicates an increase of overall circulation for the vortex pair.

Three views of another instantaneous snapshot help interpret this behavior. From the vorticity pattern shown in Figure 17, it appears that the presence of a K-H vortex makes the streamwise

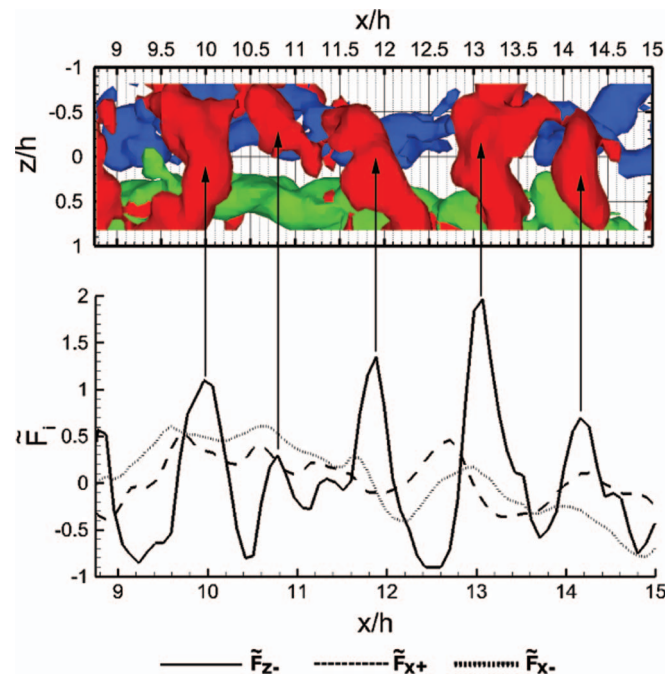


FIG. 15. The instantaneous vorticity integral distributions along streamwise direction (lower part) and the top view of the corresponding instantaneous vorticity field (upper part).

vortices approach each other. These two filaments are also accelerated towards the preceding K-H vortex (under its head) due to the effect of the focused fluid ejection. Moreover, the K-H vortex features an arc-like shape and its legs are inclined from the vertical under the strain field. As a result, in the lower region, they contribute significantly to the streamwise vorticity. In some cases, the legs of K-H vortices appear to merge with the primary streamwise vortices. Unfortunately, the spatial resolution of the measurement does not allow to explore the details of such merge activity.

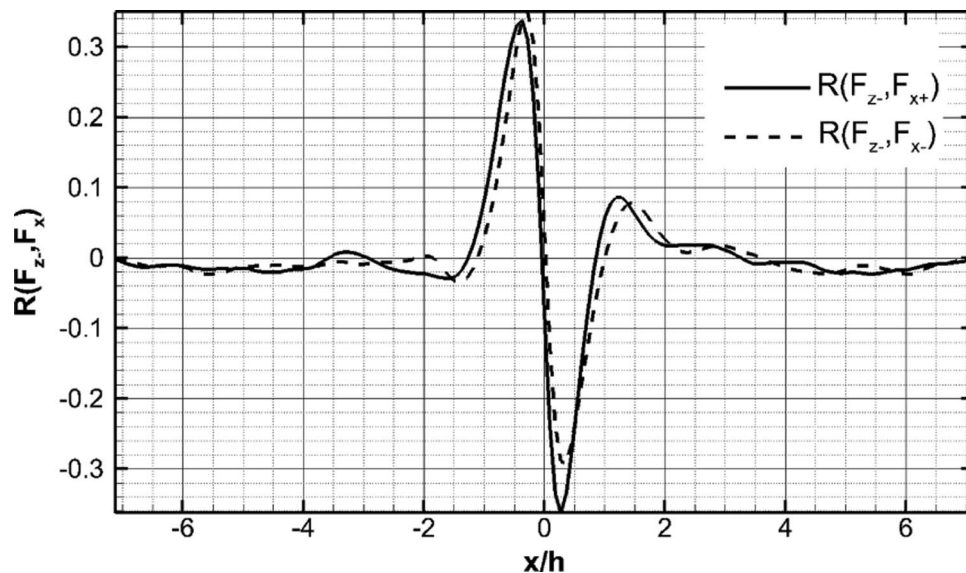


FIG. 16. Spatial cross-correlation between  $F_{z-}$  and  $F_x$ ,  $R(F_{z-}, F_x)$  is the cross-correlation coefficient.

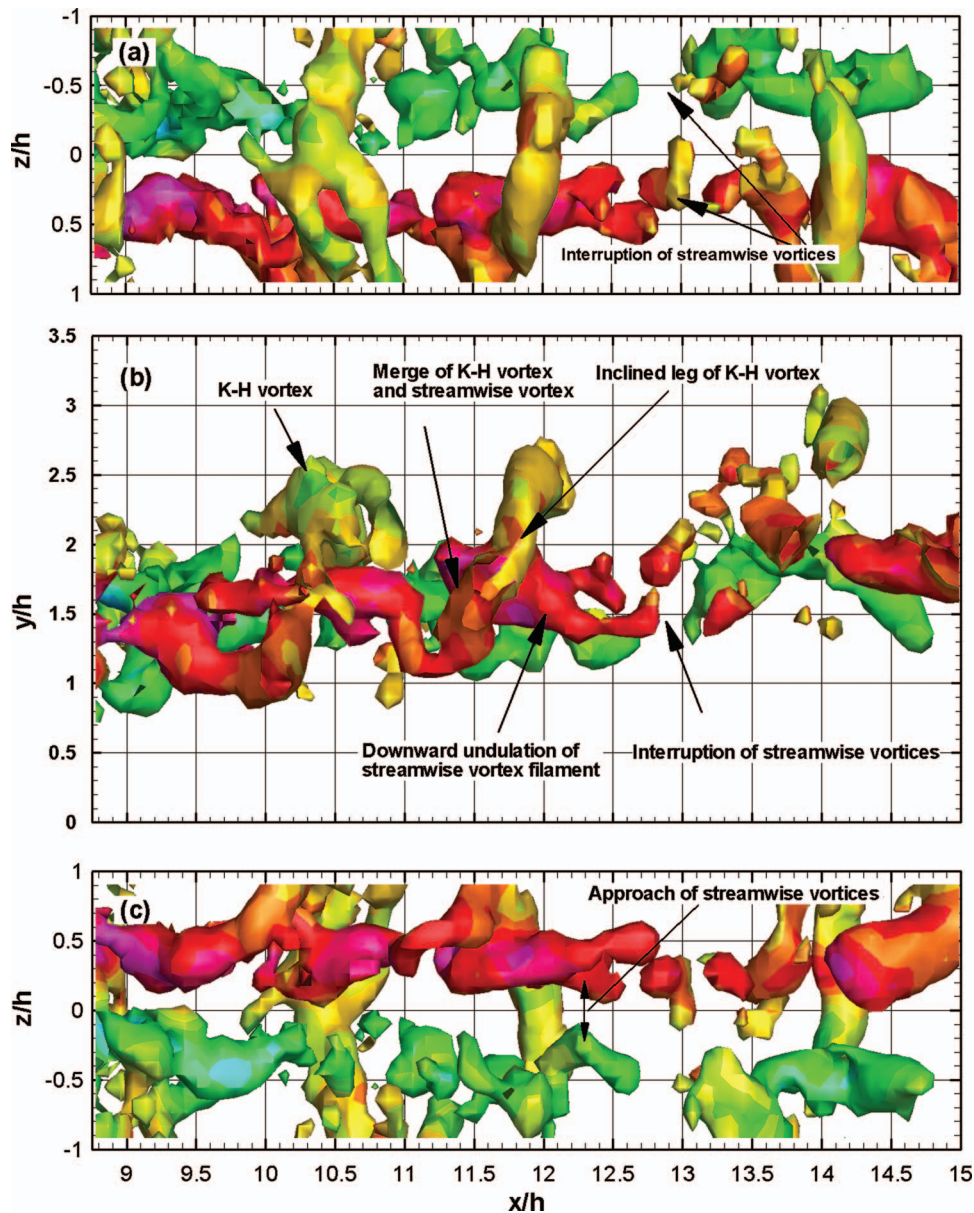


FIG. 17. Three views of the iso-surfaces of  $Q$  criterion at a certain value in a snapshot of the instantaneous flow field. The iso-surfaces are flooded by the value of streamwise vorticity  $\omega_x$ , (a) top view, (b) side view, and (c) bottom view.

Downstream of the K-H vortex head, the two streamwise vortices appear to be vigorously stretched and tilted often leading to the interruption of the vortex filament, which justifies the streamwise vorticity minimum returned by the cross-correlation analysis.

#### D. Wavelength of the K-H instability

A statistical estimate of the separation distance between neighboring K-H vortices is obtained by performing the spatial auto-correlation of spanwise vorticity  $\omega_z$ . The auto-correlation of the vorticity field at the symmetric plane gives out three distinct peaks in the correlation map. One of them is located at the center position, and is the result of the multiplication of the vorticity field itself. The other two peaks are symmetric around the central one, and they are the multiplication of the two vorticity fields with a distance shift of the wavelength. The wavelength is then calculated by measuring the distance between the central peak and one of the neighboring two.

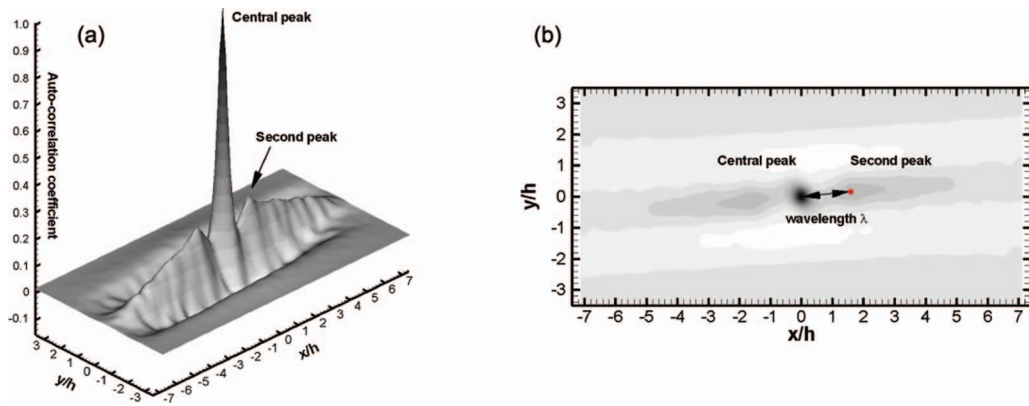


FIG. 18. Spatial auto-correlation map of  $\omega_z(x, y)$  at the symmetric plane ( $z/h = 0$ ).

The resulting wavelength  $\lambda$  of the K-H instability within the measurement domain is approximately  $1.75h$  or  $7\text{ mm}$ . The correlation map is presented in Figure 18. Conducting the analysis at several streamwise locations produces very similar results, indicating that in current measurement range no phenomenon, such as vortex pairing or breakdown, is active on the K-H vortices.

### V. TURBULENCE PROPERTIES

With the mean flow pattern and the instantaneous coherent structures established, the statistical turbulent flow properties, such as fluctuations across the circular shear layer will be characterized in this section.

#### A. RMS of the velocity field

The fluctuations are represented by the RMS values of the velocity field acquired from Measurement II, mirrored with respect to the median plane to provide a full image of the wake cross section. Three streamwise cross sections at  $x/h = 8.75, 11.25,$  and  $13.75$  (or  $x = 35, 45, 55\text{ mm}$ ) and the streamwise-wall-normal cross section at  $z/h = 0$  are selected to represent the flow. These slices are plotted in Figure 19. The plots in the first row are the contours of  $\langle u' \rangle$ , and those in the second row are contours of  $\langle v' \rangle$ .

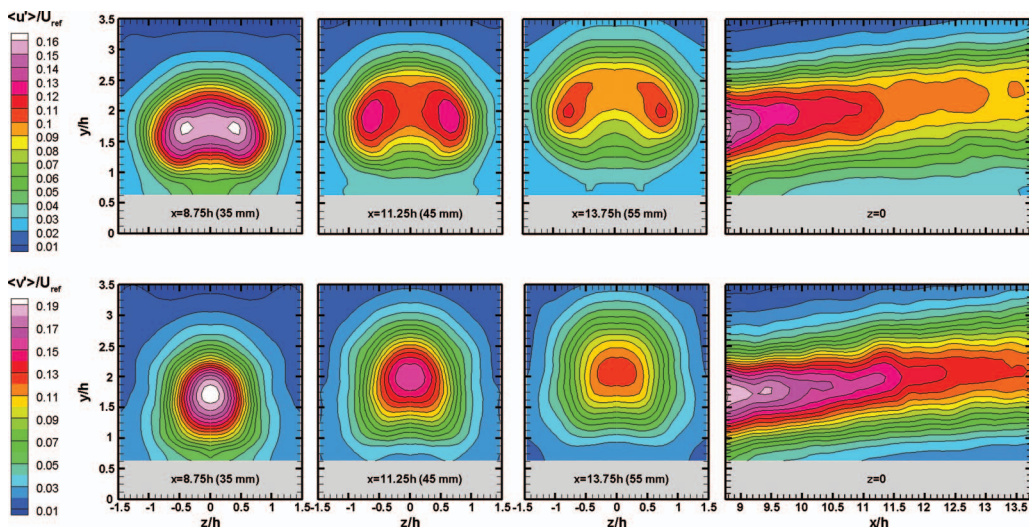


FIG. 19. Selected cross sections of contours of the RMS of  $u$  and  $v$ . The results are from Measurement II, and mirrored across the center plane ( $z/h = 0$ ) according to the symmetrical hypothesis.

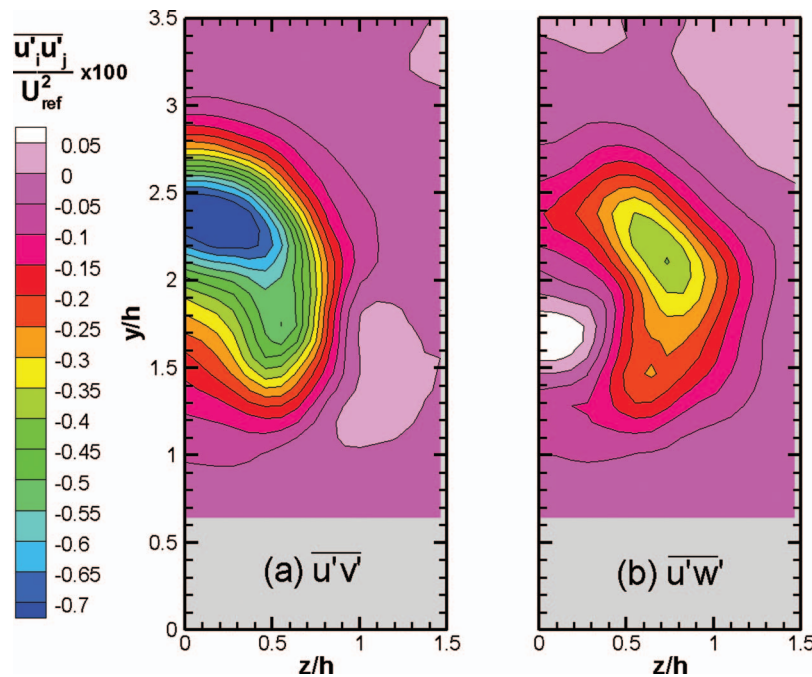


FIG. 20. Reynolds stress distributions in the cross section at  $x/h = 11.25$ ; (a) contours of  $\overline{u'v'}$  and (b) contours of  $\overline{u'w'}$ .

Larger fluctuations of both  $u$  and  $v$  can be observed inside the wake region, with peak fluctuations appearing at different positions for each component. A maximum of  $\langle u' \rangle$  appears at the location corresponding to the streamwise vortex core and reaches  $0.16U_{ref}$  at the most upstream position  $x/h = 8.75$ . The position of  $\langle u' \rangle_{max}$  confirms the meandering behavior of the streamwise vortex, which does not follow its averaged straight path, but travels along a slightly curving route. The peak of  $\langle v' \rangle$  occurs at the center of the wake and displays a magnitude of  $0.19U_{ref}$  at  $x/h = 8.75$ . This larger fluctuation of  $v$  comes from the distortion of the instantaneous upwash motion which appears as an exact wall-normal event in the averaged flow field. After traveling downstream, the fluctuations for both components decay to a lower values following the recovery of the wake region.

## B. Reynolds stress of the flow field

Turbulent mixing that takes place in the shear layer is expressed by the Reynolds shearing stresses ( $\overline{u'_i u'_j}$ ,  $i \neq j$ ). As the shear layer is generated with a circular shape in the current flow, at the top of shear layer the mixing takes place mainly along the wall-normal direction, therefore  $\overline{u'v'}$  should become negative. At the side of the wake, the flow will be mixed mainly along the spanwise direction, making  $\overline{u'w'}$  the relevant shear stress component. The distribution of the two components of the Reynolds stress at  $x/h = 11.25$  are plotted in Figure 20. The peak of  $\overline{u'v'}$  can be observed at the top part of the shear layer and reaches a magnitude of  $-0.7U_{ref}^2/100$ . At either side of the shear layer  $\overline{u'w'}$  obtains the peak at about  $y/h = 2.13$ , its magnitude is about half of that of  $\overline{u'v'}$ . With different Reynolds stress at different positions, anisotropy of turbulent strength can thus be concluded towards the circular shear layer. Due to the weaker Reynolds stress at both sides, the mixing across the horizontal direction takes place with less strength, accordingly the K-H instability is produced with less intensity.

It is also worthwhile to pay some attention to the Reynolds stresses at the bottom part of the circular shear layer. Since no peak value is observed there, the turbulence strength is not as prominent as those in the top part. It could be attributed to the weaker shear layer at the bottom part due to the presence of the wall.

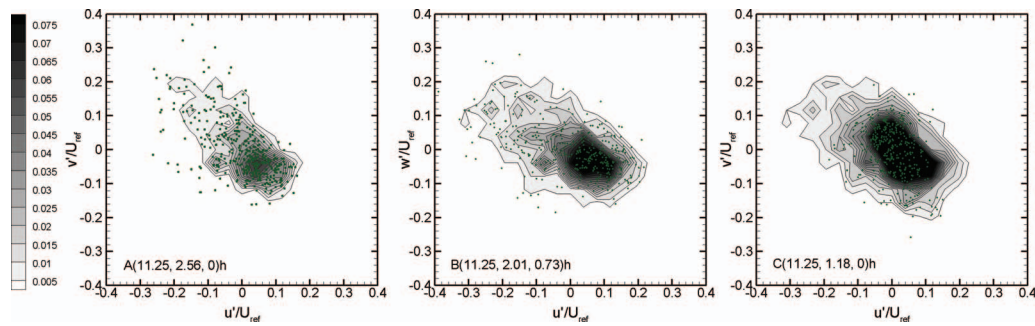


FIG. 21. Scatter plots of the components of velocity fluctuation at three positions, their joint pair distribution function is also overlaid.

To illustrate the turbulence of the wake in more detail, three positions are chosen to represent the typical locations, they are:  $A(11.25, 2.58, 0)h$  in the top part of shear layer,  $B(11.25, 2.01, 0.73)h$  in the side part of the shear layer, and  $C(11.25, 1.18, 0)h$  in the bottom part of the wake region. The scatter plots of velocity fluctuations at these positions are depicted in Figure 21. Due to the mixing that happens at different directions in the circular shear layer,  $u'$  and  $v'$  are chosen as the variables at  $A$  and  $C$ , while  $u'$  and  $w'$  are considered at  $B$ . Elliptically shaped distributions of fluctuation components with concentration in the fourth quadrant ( $Q4$ ) occur at both  $A$  and  $B$ . The  $Q4$  event producing a negative Reynolds stress is a sign to intensification of the exchange between flows of different momentum, i.e., mixing. At the third position  $C$ , although the distribution has a slight elongated major axis forming a nearly  $45^\circ$  angle with the vertical axis, the distribution becomes more compact.

### C. Conditional average of the vorticity field

The analysis of the vortex features from instantaneous realizations remains difficult due to the large spatial fluctuations caused by the flow unsteadiness. Therefore, an ensemble average of a K-H vortex is obtained by using an indicator function of the spanwise vorticity  $\omega_z$ . The detected vortices are aligned according to the position of the vorticity peak and then ensemble averaged. The procedure is repeated at three locations spaced by a distance equal to the K-H wavelength  $\lambda$ . The results from the different locations are spatially merged and represent a visualization of a train of K-H vortices enveloping the streamwise vortex pair. Figure 22 shows the iso-surfaces of

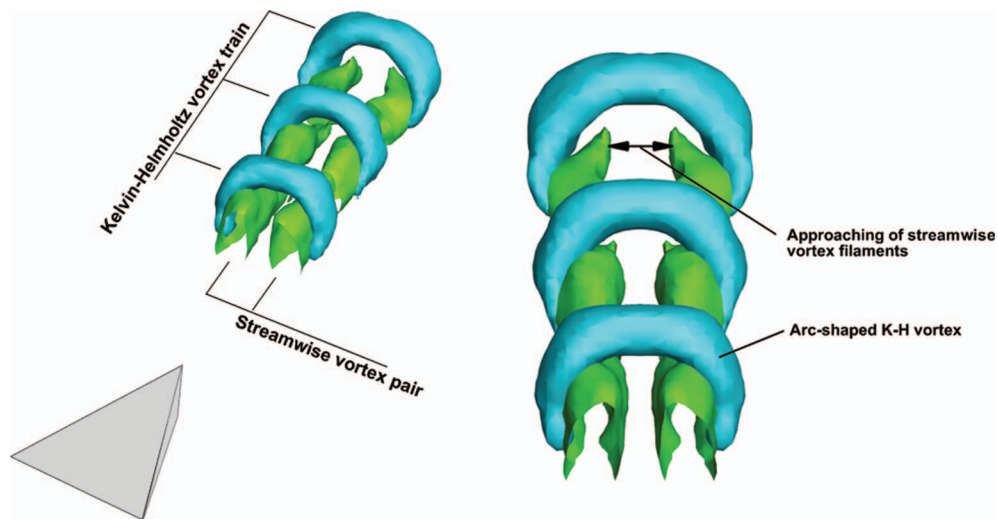


FIG. 22. Conditionally averaged vorticity distribution in the wake of a micro-ramp. Vorticity iso-surfaces of streamwise component  $\omega_x$  (green) and spanwise-wall-normal component  $\sqrt{\omega_y^2 + \omega_z^2}$  (light blue).

vorticity decomposed in the streamwise component  $\omega_x$ , and the complementary part  $\sqrt{\omega_y^2 + \omega_z^2}$ . The former represents the primary vortex pair, whereas the latter identifies the arc-shaped K-H vortices. Most of the fluctuations observed in the instantaneous flow visualization are not present in this conditional average. Nevertheless, the statistical analysis returns the arc-shaped vortices with a more inclined leg region, which merges with the streamwise vortices. The latter appear to be undulated under the action of the K-H vortex induced flow (vortex pair spacing is larger upstream and smaller downstream of the K-H vortex.). Finally, one can also observe that the strength of the streamwise vortices is decreased immediately downstream of the head region of a K-H vortex. These conclusions are consistent with the observation inferred from the instantaneous vorticity fields. In contrast, the conditional average cannot return any information on the phenomenon of the unsteady vortex meandering because spanwise oscillations of the vortex system would be averaged out in the present procedure.

## VI. CONCLUSIONS

An experimental study has been carried out to investigate the three-dimensional instantaneous organization of the flow generated by a single micro-ramp in a Mach 2.0 supersonic boundary layer using tomographic PIV. Tomographic PIV has proven to be a well-suited approach for investigating the flow generated by a micro-ramp. It reduces the complexity and ambiguity of interpreting a three-dimensional flow organization from cross-sectional visualizations alone, through providing instantaneous volumetric information.

The measurements agree qualitatively with previous studies that show that the mean flow displays a streamwise wake region coming from the trailing edge of the micro-ramp, encompassed by a circular shear layer at its outer edge. A counter-rotating vortex pair which is symmetrical to the center plane of the micro-ramp is produced, and contained within the wake. Both the wake and vortices are lifted when travelling downstream.

With regard to its instantaneous structure, the flow exhibits features with significant differences to the mean organization. A train of arc-shaped vortices is produced through the Kelvin-Helmholtz instability occurring in the approximately circular shear layer that bounds the wake. These K-H vortices do not show up in the mean flow field because of the averaging process.

The streamwise counter-rotating vortex pair still persists in the instantaneous flow, however, they exhibit an undulating behavior. The two streamwise vortex cores tend to become closer under the head of K-H vortex due to the ejection event resulting from the K-H vortex. The arc-shaped K-H vortices are also influential to the instantaneous flow pattern. The vortex rotates in the clockwise direction; as a result, on top of the vortex there is local acceleration, with local deceleration being below the vortex accordingly. These local activities produce local high-speed and low-speed regions outside and inside the wake respectively, which also tend to display as the shape of arc. Since the strength of the K-H vortex varies, the corresponding local high-speed and low-speed regions may appear only partially. The interactions between the streamwise vortices and K-H vortices make the flow inside the wake rather complex and the low-speed region hence exhibits variations.

The turbulence properties derived from the statistics confirms the large-scale fluctuations exhibit by the instantaneous flow structures. Larger magnitudes of  $\langle u' \rangle$  and  $\langle v' \rangle$  are achieved because of unstable wake region and the fluctuating upwash, respectively. Higher Reynolds stress components are produced at the edge of the deficit region signifying pronounced shearing event happened there.

## ACKNOWLEDGMENTS

This work is sponsored by the Chinese Scholarship Council.

<sup>1</sup>J. M. Delery, "Shock wave/turbulent boundary layer interaction and its control," *Prog. Aerosp. Sci.* **22**, 209 (1985).

<sup>2</sup>J. C. Lin, "Review of research on low-profile vortex generators to control boundary-layer separation," *Prog. Aerosp. Sci.* **38**, 389 (2002).

- <sup>3</sup> M. Rybalko, H. Babinsky, and E. Loth, "VGs for a normal SBLI with a downstream diffuser," AIAA Paper No. 2010-4464, 2010.
- <sup>4</sup> A. Jirasek, "Vortex-generator model and its application to flow control," *J. Aircr.* **42**, 1486 (2005).
- <sup>5</sup> K. S. Bohannon, "Passive flow control on civil aircraft flaps using sub-boundary layer vortex generators in the AWIATOR programme," AIAA Paper No. 2006-2858, 2006.
- <sup>6</sup> D. S. Galbraith, M. C. Galbraith, M. G. Turner, P. D. Orkwis, and A. Apyan, "Preliminary numerical investigation of a Mach 3 inlet configuration with and without aspiration and micro-ramps," AIAA Paper No. 2010-1095, 2010.
- <sup>7</sup> B. H. Anderson, H. Tinapple, and L. Surber, "Optimal control of shock wave turbulent boundary layer interactions using micro-array actuation," AIAA Paper No. 2006-3197, 2006.
- <sup>8</sup> S. M. Hirt and B. H. Anderson, "Experimental investigation of the application of microramp flow control to an oblique shock interaction," AIAA Paper No. 2006-3197, 2006.
- <sup>9</sup> T. Herges, E. Kroecker, G. Elliott, and C. Dutton, "Micro-ramp flow control of normal shock/boundary layer interactions," *AIAA J.* **48**, 2529 (2010).
- <sup>10</sup> S. Lee, M. K. Goettke, and E. Loth, "Microramps upstreams of an oblique-shock/boundary-layer interaction," *AIAA J.* **48**, 104 (2010).
- <sup>11</sup> Q. Li and C. Liu, "LES for supersonic ramp control flow using MVG at  $M = 2.5$  and  $Re_\theta = 1440$ ," AIAA Paper No. 2010-592, 2010.
- <sup>12</sup> S. Lee, E. Loth, N. J. Georgiadis, and J. R. DeBonis, "Effect on Mach number on flow past microramps," *AIAA J.* **49**, 97 (2011).
- <sup>13</sup> S. Lee and E. Loth, "Supersonic boundary-layer interactions with various micro-vortex generator geometries," *Aeronaut. J.* **113**, 683 (2009).
- <sup>14</sup> Q. Li and C. Liu, "Numerical investigations on the effects of the declining angle of the trailing-edge of MVG," *J. Aircr.* **47**, 2086 (2010).
- <sup>15</sup> H. Babinsky, Y. Li, and C. W. Pitt Ford, "Microramp control of supersonic oblique shock-wave/boundary-layer interactions," *Aeronaut. J.* **47**, 668 (2009).
- <sup>16</sup> P. L. Blinde, R. A. Humble, B. W. van Oudheusden, and F. Scarano, "Effects of micro-ramps on a shock wave/turbulent boundary layer interaction," *Shock Waves* **19**, 507 (2009).
- <sup>17</sup> F. K. Lu, A. J. Pierce, and Y. Shih, "Experimental study of near wake of micro vortex generators in supersonic flow," AIAA Paper No. 2010-4623, 2010.
- <sup>18</sup> W. J. Greta and C. R. Smith, "The flow structure and statistics of a passive mixing tab," *J. Fluids Eng.* **115**, 255 (1993).
- <sup>19</sup> W. Yang, H. Meng, and J. Sheng, "Dynamics of hairpin vortices generated by a mixing tab in a channel flow," *Exp. Fluids* **30**, 705 (2001).
- <sup>20</sup> G. E. Elsinga, F. Scarano, B. Wieneke, and B. W. van Oudheusden, "Tomographic particle image velocimetry," *Exp. Fluids* **41**, 933 (2006).
- <sup>21</sup> G. E. Elsinga, R. J. Adrain, B. W. van Oudheusden, and F. Scarano, "Three-dimensional vortex organization in a high-Reynolds-number supersonic turbulent boundary layer," *J. Fluid Mech.* **644**, 35 (2010).
- <sup>22</sup> R. A. Humble, G. E. Elsinga, F. Scarano, and B. W. van Oudheusden, "Three-dimensional instantaneous structure of a shock wave/turbulent boundary layer interaction," *J. Fluid Mech.* **622**, 33 (2009).
- <sup>23</sup> R. A. Humble, F. Scarano, and B. W. Oudheusden, "Particle image velocimetry measurement of a shock wave/turbulent boundary layer interaction," *Exp. Fluids* **43**, 173 (2007).
- <sup>24</sup> D. Ragni, F. F. J. Schrijer, B. W. van Oudheusden, and F. Scarano, "Particle tracer response across shocks measured by PIV," *Exp. Fluids* **50**, 53 (2011).
- <sup>25</sup> F. F. J. Schrijer and F. Scarano, "Effect of predictor-corrector filtering on the stability and spatial resolution of iterative PIV interrogation," *Exp. Fluids* **45**, 927 (2008).
- <sup>26</sup> S. Dong and H. Meng, "Flow past a trapezoidal tab," *J. Fluid Mech.* **510**, 219 (2004).
- <sup>27</sup> F. K. Lu, A. J. Pierce, Y. Shih, C. Liu, and Q. Li, "Experimental and numerical study of flow topology past micro vortex generators," AIAA Paper No. 2010-4463, 2010.
- <sup>28</sup> R. Elavarasan and H. Meng, "Flow visualization study of the role of coherent structures in a tab wake," *Fluid Dyn. Res.* **27**, 183 (2000).
- <sup>29</sup> Q. Li, Y. Yang, X. Wang, and C. Liu, "The interaction between vortex rings and oblique shocks by the MVG controlled ramp flow at  $M = 2.5$ ," AIAA Paper No. 2011-861, 2011.